

Alma Mater Studiorum Università di Bologna
Archivio istituzionale della ricerca

Disclosing the Role of Gold on Palladium – Gold Alloyed Supported Catalysts in Formic Acid Decomposition

This is the final peer-reviewed author's accepted manuscript (postprint) of the following publication:

Published Version:

Barlocco I., Capelli S., Lu X., Bellomi S., Huang X., Wang D., et al. (2021). Disclosing the Role of Gold on Palladium – Gold Alloyed Supported Catalysts in Formic Acid Decomposition. CHEMCATCHEM, 13, 4210-4222 [10.1002/cctc.202100886].

Availability:

This version is available at: <https://hdl.handle.net/11585/844509> since: 2023-05-08

Published:

DOI: <http://doi.org/10.1002/cctc.202100886>

Terms of use:

Some rights reserved. The terms and conditions for the reuse of this version of the manuscript are specified in the publishing policy. For all terms of use and more information see the publisher's website.

This item was downloaded from IRIS Università di Bologna (<https://cris.unibo.it/>).
When citing, please refer to the published version.

(Article begins on next page)

This is the final peer-reviewed accepted manuscript of:

Ilaria Barlocco, Sofia Capelli, Xiuyuan Lu, Silvio Bellomi, Xiaohui Huang, Di Wang, Laura Prati, Nikolaos Dimitratos, Alberto Roldan, and Alberto Villa, Disclosing the Role of Gold on Palladium – Gold Alloyed Supported Catalysts in Formic Acid Decomposition, ChemCatChem 2021, 13, 4210–4222.

The final published version is available online at:
<https://doi.org/10.1002/cctc.202100886>

Terms of use:

Some rights reserved. The terms and conditions for the reuse of this version of the manuscript are specified in the publishing policy. For all terms of use and more information see the publisher's website.

<https://onlinelibrary.wiley.com/page/journal/18344461/homepage/permissions.html>

This item was downloaded from IRIS Università di Bologna (<https://cris.unibo.it/>)

When citing, please refer to the published version.

Disclosing the role of Gold on Palladium - Gold alloyed supported catalysts in formic acid decomposition

Ilaria Barlocco,^[a] Sofia Capelli,^[a] Xiuyuan Lu,^[b] Silvio Bellomi,^[a] Xiaohui Huang,^[c] Di Wang,^{[c], [d]} Laura Prati,^[a] Nikolaos Dimitratos,^[e] Alberto Roldan,^{*,[b]} Alberto Villa,^{*,[a]}

[a] I. Barlocco, Dr. S. Capelli, S. Bellomi, Prof. L. Prati, Prof. A. Villa*
Dipartimento di Chimica
Università degli Studi di Milano
Via Golgi 19, 20133 Milano, Italy
E-mail: alberto.villa@unimi.it

[b] X. Lu, Dr. A. Roldan*
Cardiff Catalysis Institute, School of Chemistry
Cardiff University
Main Building, Park Place, CF10 3AT, Cardiff, United Kingdom
E-mail: RoldanMartinezA@cardiff.ac.uk

[c] X. Huang, Prof. D. Wang
Institute of Nanotechnology
Karlsruhe Institute of Technology
Hermann-von-Helmholtz-Platz 1, 76344 Eggenstein-Leopoldshafen, Germany

[d] Dr. D. Wang
Karlsruhe Nano Micro Facility (KNMF)
Karlsruhe Institute of Technology
Hermann-von-Helmholtz-Platz 1, 76344 Eggenstein-Leopoldshafen, Germany

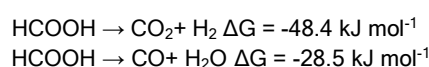
[e] Prof. N. Dimitratos
Dipartimento di Chimica Industriale e dei Materiali
ALMA MATER STUDIORUM Università di Bologna
Viale Risorgimento 4, 40136 Bologna, Italy

Supporting information for this article is given via a link at the end of the document.

Abstract: Herein, we report the synthesis of preformed bimetallic Pd-Au nanoparticles supported on carbon nanofibers with different Pd:Au atomic ratio (nominal molar ratio: 8-2, 6-4, 4-6, 2-8) and the corresponding Pd and Au monometallic catalysts by sol immobilization method. The obtained materials were characterized thoroughly by Transmission Electron Microscopy (TEM), X-ray photoelectron spectroscopy (XPS) and inductively coupled plasma optical emission spectroscopy (ICP - OES). The catalytic performances of the Pd-Au catalysts were evaluated in the aqueous phase dehydrogenation of formic acid (FA) at room temperature obtaining enhanced activity, stability and selectivity compared to the monometallic systems. In particular, Pd₆Au₄ and Pd₈Au₂ showed the best combination of catalytic properties, i.e. high selectivity to H₂ and improved catalytic stability. Density functional theory (DFT) calculations on Pd₁₅, Au₁₅ and Pd₉Au₆ clusters supported on a carbon sheet were then simulated to provide atomic level understanding to the beneficial effect of gold observed in the experimental results. Au₁₅ barely adsorb FA, while Pd₁₅ possesses an adsorption energy higher than the Pd₉Au₆ one. Dehydrogenation and dehydration pathways were followed on all these models. For Pd₉Au₆, the most favourable route was the formation of carbon dioxide and hydrogen. Analysis of the electronic structures was also performed on the different models showing a stronger interaction between the bimetallic system and the support proving the alloy superior stability.

Introduction

Benign and sustainable alternative energy sources are needed to mitigate the increasing dependence on fossil fuels and their high environmental impact. Hydrogen is recognised as an efficient alternative energy carrier because of its high energy density and innocuous products upon utilisation^[1]. Despite this, its direct use is hindered due to the shortage of economically and safe hydrogen storage technologies^[2] and, therefore, alternative methods to store and transport it is of paramount importance^[3-6]. In line with the U.S. Department of Energy, formic acid (FA) is an attractive hydrogen carrier due to its high volumetric hydrogen content (4.4 wt% of H₂), non-toxic character, and stability in liquid phase at standard temperature and pressure^[7]. Furthermore, FA is readily accessible from catalytic conversion of biomass^[8,9]. A controlled catalytic FA dehydrogenation is required to release hydrogen on-demand^[10-12], nevertheless, the decomposition of FA occurs in two competing pathways:



The first and most exothermic route is the desired dehydrogenation reaction; it produces hydrogen and carbon dioxide closing the carbon-neutral cycle. The second pathway is the dehydration reaction producing carbon monoxide^[13].

Among all the studied heterogeneous catalysts, Pd/C have been deeply investigated because of its superior activity at room temperature. On the other hand, the examined Pd/C catalysts quickly deactivate because of the high affinity with poisoning intermediates, such as CO, which blocks the active sites^[14,15]. The poor stability dissuades industrialists from further examination and implementation.

To overcome the poisoning, it has been shown that the introduction of a second metal forming alloy catalysts, especially gold, overcame this problem and generates also ultrapure hydrogen at low temperature^[16-18].

Xing *et al.* have shown that, unlike Pd/C catalysts, PdAu/C alloy catalysts inhibits the problems caused by CO poisoning. This effect is attributed to the bimetallic catalyst's nature allowing higher activity and selectivity with respect of monometallic ones. Furthermore, they have demonstrated that increasing the amount of Au in the alloy promotes the NP's lattice expansion due to the strain effect of the second metal. At high Au:Pd ratios, the electron transfer from Au to Pd dominates and the synergistic effect controls the activity of the catalyst^[19]. An optimized activity and stability is obtained with a suitable balance between the internal lattice strain and the synergistic effects resulting in maximised activity against molar ratios' Volcano plot^[20,21]. Li *et al.*^[22] studied Pd₅₅ and Pd_xAu_(55-x) clusters via density functional theory (DFT). They found that gold can weakly bond atomic hydrogen leading to an easier hydrogen production on bimetallic catalysts. Yoon *et al.*^[17] combined experimental and DFT techniques in order to disclose the synergistic and ensemble effects of gold in PdAu bimetallic catalysts. Different PdAu(111) modelled alloys were prepared and the importance of this two factors on the catalytic activity in FA decomposition (FAD) reaction was confirmed. Karatas *et al.* have shown the enhanced stability of PdAu nanoparticles (NPs) against leaching and agglomeration when supported on MnO_x, providing a superior efficiency for the FA dehydrogenation reaction^[23]. Moreover, it was shown that alloying Au with Pd can also improve the catalytic stability in alcohol oxidation^[24,25].

However, a detailed study on the interaction between PdAu clusters and carbonaceous surface is still missing. Indeed, in this study 15 atoms clusters of Pd, Au and PdAu on a graphene surface were modelled from bulk and superficial analyses, in order to precisely establish the principles of their performance. Similarly, the rationalization between the role of interfacial and bulk metal atoms in the catalytic activity in FAD reaction has not been achieved. In fact, it is well known that the interaction between support and metal plays a central role in the catalysts' performance. Moreover, a detailed mechanistic investigation on the effect of the addition of gold to palladium not only on the activity, but also on selectivity and stability of these bimetallic catalysts is not reported yet. Herein, we report experimental and theoretical details on the enhanced catalytic behaviour of PdAu

bimetallic catalysts in the FAD process under mild reaction conditions. Activity, selectivity and stability tests were performed using Pd-Au bimetallic catalysts with different Pd/Au molar ratios supported on high temperature (3000 °C) heat treated (HHT) carbon nanofibers. Fresh and used catalysts were then characterized using transmission electron microscopy (TEM) and X-ray photoelectron spectroscopy (XPS) in order to establish a correlation between the morphology of the materials and their catalytic activity. The combination of experiments and simulations allowed us to disclose the beneficial effect of the second metal regarding the superior activity, stability and selectivity of the bimetallic systems.

Results and Discussion

Main Text Paragraph. Monometallic and bimetallic catalysts with different Pd:Au molar ratio were prepared via sol-immobilization technique, using PVA as capping agent and NaBH₄ as reducing agent. High temperature heat-treated carbon nanofibers (HHT CNFs) were used as carbonaceous support. Previous studies have shown that this type of CNFs lead to an enhanced activity in FAD reaction in the presence of small and homogeneously dispersed Pd nanoparticles^[26,27].

TEM-STEM results. TEM analyses were performed in order to investigate the structures of the materials, i.e. average particle size, particle size distribution and bulk gold-palladium atomic ratio. Monometallic (1%Pd@HHT and 1%Au@HHT) and bimetallic (1%Pd_xAu_y@HHT) catalysts were characterized at the sub-nanometric scale by TEM. 1%Pd@HHT shows an average particle size of 3.9 nm (Table 1)^[28]. All bimetallic catalysts appear to have a similar average particle size, between 2.9 and 4 nm (Table 1), with a narrow particle size distribution (Figure 1b - 4b). Figures 1-4 show the representative results of STEM and EDX analysis on the single NPs for Pd_xAu_y bimetallic systems. The NPs are well dispersed on the support. By STEM-EDS spectrum imaging, we evaluated the amount of Pd and Au on individual metal NPs and observed a good agreement between the nominal and the actual atomic ratio for all the bimetallic catalysts, except for Pd₂Au₈ catalyst (Table 1). For this catalyst, the Au/Pd atomic ratio calculated by EDX is higher than the nominal one, in fact, Au/Pd_{EDX} (8.70/1.30) ratio is equal to 6.69 while Au/Pd_{nom} (8/2) corresponds to 4 (Table 1, row 6). This discrepancy can be attributed to the presence of some segregated palladium nanoparticles. STEM-HAADF images and STEM-EDS maps of single nanoparticles suggested that the catalysts consist in Au-Pd alloyed systems (Figures 1-4).

Table 1. Results of TEM-EDX analysis.

	Pd: Au Nominal	Pd : Au EDX	Au/Pd _{nom}	Au/Pd _{EDX}	Average particle size (nm)
1%Pd@HHT	-	-			3.9 ± 1.2
1%Pd ₈ Au ₂ @HHT	8.00 : 2.00	8.35 : 1.65	0.25	0.20	3.5 ± 0.9
1%Pd ₆ Au ₄ @HHT	6.00 : 4.00	5.86 : 4.14	0.67	0.71	2.9 ± 0.7
1%Pd ₄ Au ₆ @HHT	4.00 : 6.00	4.46 : 5.54	1.50	1.24	4.0 ± 0.8
1%Pd ₂ Au ₈ @HHT	2.00 : 8.00	1.30 : 8.70	4.00	6.69	3.1 ± 0.6
1%Au@HHT	-	-			3.4 ± 1.2
1%Pd ₈ Au ₂ @HHT used	8.00 : 2.00	8.06 : 1.94	0.25	0.24	3.9 ± 1.1
1%Pd ₆ Au ₄ @HHT used	6.00 : 4.00	5.83 : 4.17	0.67	0.70	3.1 ± 0.8

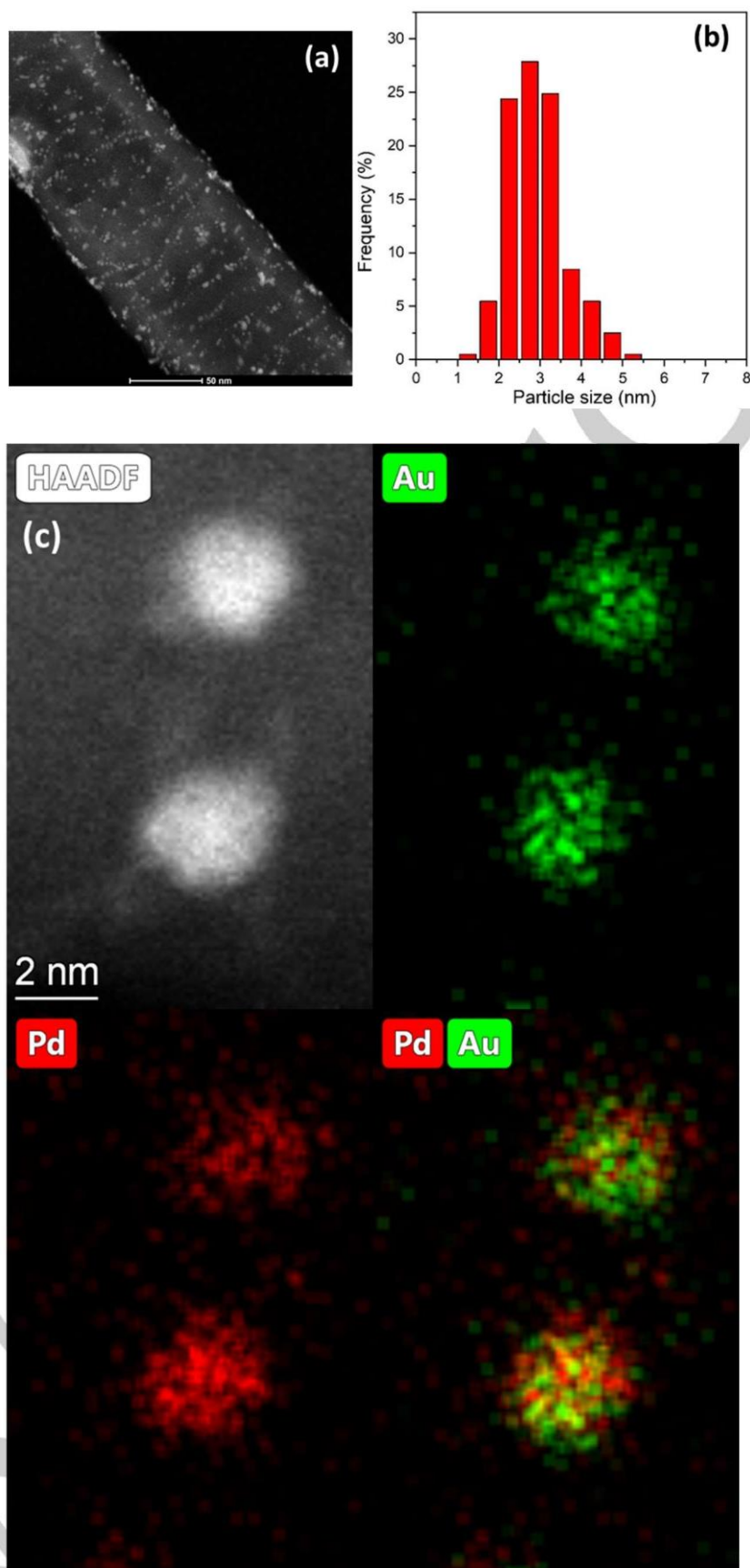


Figure 1. a) STEM-HAADF image of 1%Pd₆Au₄@HHT catalyst, b) particle size distribution and c) STEM-EDS maps of single nanoparticles.

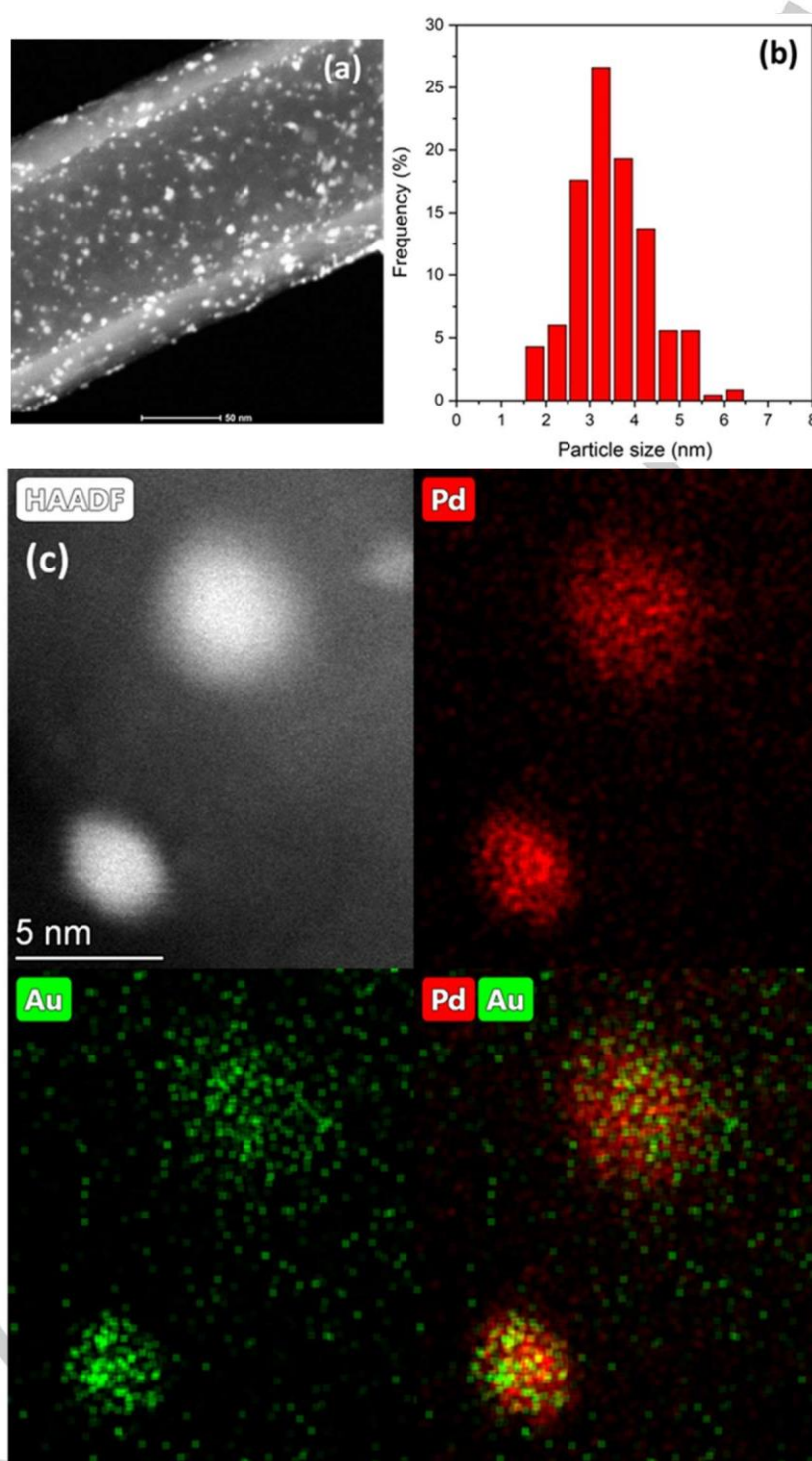


Figure 2. a) STEM-HAADF image of 1%Pd₈Au₂@HHT catalyst, b) particle size distribution and c)

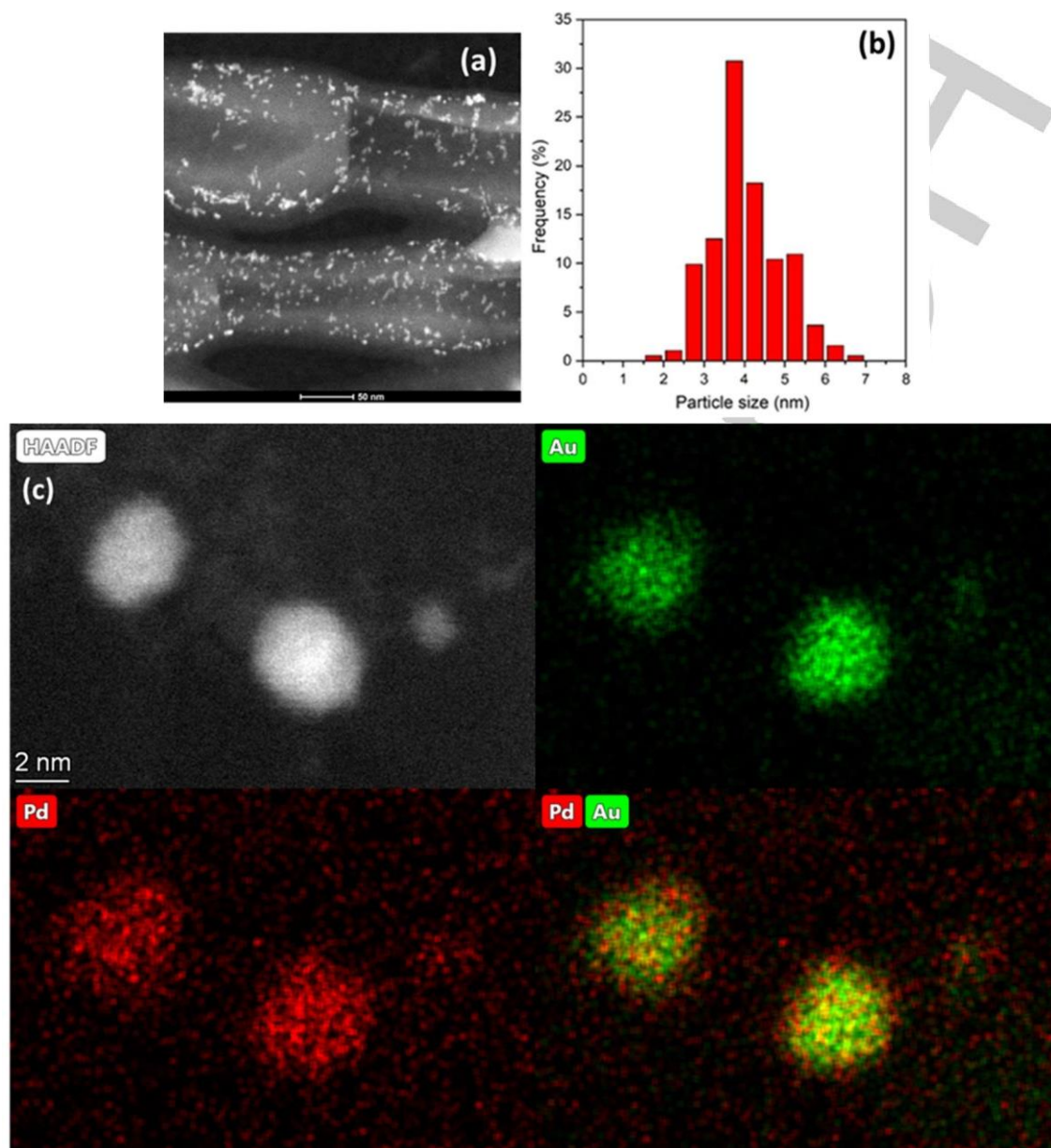


Figure 3. a) STEM-HAADF image of 1%Pd₄Au₆@HHT catalyst, b) particle size distribution and c) STEM-EDS maps of single nanoparticles.

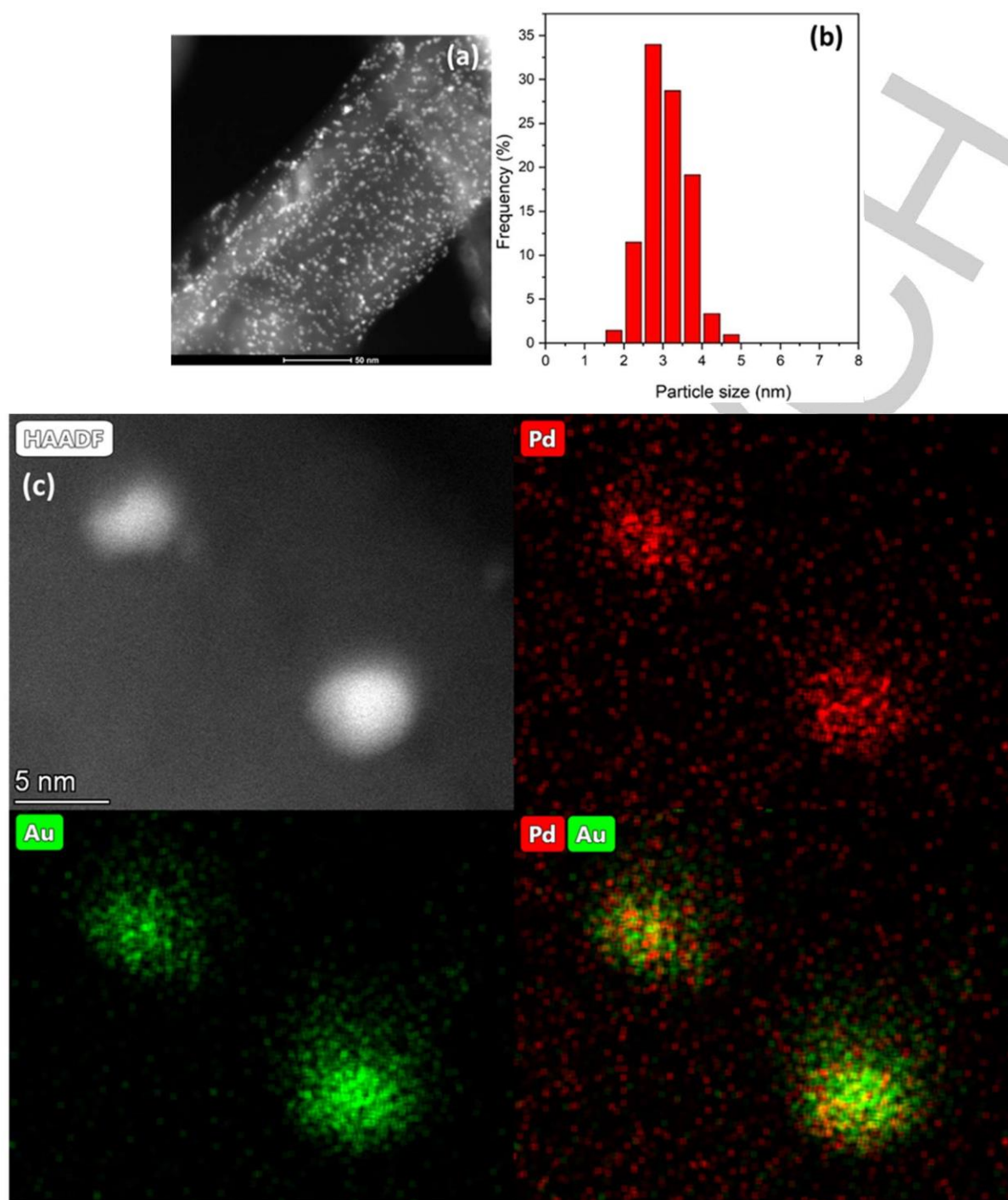


Figure 4. a) STEM-HAADF image of 1%Pd₂Au₈@HHT catalyst, b) particle size distribution and c) STEM-EDS maps of single nanoparticles.

XPS results. In order to obtain information of the surface composition (e.g., oxidation state, superficial atomicity, and exposed gold-palladium ratio), X-ray photoelectron spectroscopy was performed. From the survey spectra obtained by XPS analysis, we detected 4 main species: C 1s (284.24-284.59 eV), O 1s (532.24-532.59 eV), Au 4f (83.31-84.24 eV), and Pd 3d (335.40-337.59 eV). The Au/Pd surface atomic ratio measured by XPS is lower than the corresponding bulk Au/Pd measured by

EDX, which may suggest surface enrichment of Pd atoms on the bimetallic nanoparticles (Table 2). This outcome confirms the result obtained using TEM analysis, which previously shows an enrichment of Pd on the surface.

The high-resolution spectra of Au 4f (Figure S1) and Pd 3d (Figure S2) were deconvoluted. Au 4f shows two main species, which were assigned to Au⁰ and Au^{δ+}. The peaks at 84.11-84.32 eV and 85.30-85.62 eV were ascribed to Au⁰ and Au^{δ+}, respectively

FULL PAPER

(Table 3, Column3 and 4). The higher is the amount of Pd used during the catalyst synthesis, the lower is the amount of Au⁰. This phenomenon can be attributed to the transfer of electron from gold to palladium, as it has been shown in reference^[29]. In particular, the higher the amount of gold, the higher the Au⁰ amount meaning a transfer of electron from gold to palladium. In the high-resolution spectra of Pd 3d, three different peaks were detected. Two main species were identified: Pd⁰ and Pd^{II} in a B.E. range of 335.50-336.70 eV and 337.00-338.60 eV, respectively.

Moreover, a satellite peak of Pd was found between 342.30 eV and 348.11 eV. From the relative area value of the Pd species the Pd⁰/Pd^{II} ratio was calculated. (Table 3, Column 10). Furthermore, a decrease in the binding energy of the Pd⁰ peak (Δ B.E. between 1.1 -1.2 eV) in bimetallic catalysts was observed. This modification of B.E. can be attributed to an electronic interaction between the two metals, in particular to a donation of electron from gold to palladium^[29].

Table 2. Results of survey spectra.

		C 1s	O 1s	Au 4f	Pd 3d	Au/Pd _{nom}	Au/Pd _{xps}	Au/Pd _{EDX}
1%Au@HHT	B.E. (eV)	284.31	532.31	83.31	-	-	-	-
	%At.	97.80	2.10	0.10	-	-	-	-
1%Pd ₂ Au ₈ @HHT	B.E. (eV)	284.50	532.50	83.50	335.50	-	-	-
	%At.	98.33	1.40	0.20	0.07	4.00	2.86	6.69
1%Pd ₄ Au ₆ @HHT	B.E. (eV)	284.32	532.32	84.32	335.52	-	-	-
	%At.	96.20	3.10	0.32	0.30	1.50	1.07	1.24
1%Pd ₆ Au ₄ @HHT	B.E. (eV)	284.40	532.40	83.40	335.40	-	-	-
	%At.	95.50	3.50	0.39	0.65	0.67	0.60	0.71
1%Pd ₈ Au ₂ @HHT	B.E. (eV)	284.24	532.24	84.24	336.24	-	-	-
	%At.	91.18	7.30	0.14	1.31	0.25	0.11	0.20
1%Pd@HHT	B.E. (eV)	284.59	532.59	-	337.59	-	-	-
1%Pd ₆ Au ₄ @HHT	B.E. (eV)	284.51	532.51	83.51	337.51	-	-	-
used	%At.	97.29	2.47	0.08	0.16	0.67	0.50	0.70
1%Pd ₈ Au ₂ @HHT	B.E. (eV)	284.30	532.30	83.30	337.30	-	-	-
used	%At.	94.97	4.85	0.02	0.16	0.25	0.13	0.24

Table 3. Results of high resolution XPS spectra.

	Au 4f			Pd 3d			
	Au ⁰	Au ⁵⁺	Au ⁰ /Au ⁵⁺	Pd ⁰	Pd ^{II}	Pd _{sat}	Pd ⁰ /Pd ^{II}
1%Au@HHT	B.E. (eV)	84.22	85.60	B.E. (eV)	-	-	-
	%At.	90.10	9.90	%At.	-	-	-
1%Pd ₂ Au ₈ @HHT	B.E. (eV)	84.21	85.45	B.E. (eV)	335.50	337.20	342.30
	%At.	76.04	23.96	%At.	61.85	29.43	8.71
1%Pd ₄ Au ₆ @HHT	B.E. (eV)	84.15	85.30	B.E. (eV)	335.50	337.20	342.30

	%At.	67.66	32.34	2.09	%At.	79.99	16.84	3.17	4.75
1%Pd ₆ Au ₄ @HHT	B.E. (eV)	84.32	85.62		B.E. (eV)	335.60	337.00	342.50	
	%At.	67.80	32.20	2.11	%At.	67.05	18.77	14.18	3.57
1%Pd ₈ Au ₂ @HHT	B.E. (eV)	84.11	85.31		B.E. (eV)	335.60	337.10	347.10	
	%At.	50.77	49.23	1.03	%At.	68.52	21.82	9.66	3.14
1%Pd@HHT	B.E. (eV)	-	-		B.E. (eV)	336.70	337.80	348.11	
	%At.	-	-		%At.	80.68	7.94	11.38	10.16
1%Pd ₆ Au ₄ @HHT	B.E. (eV)	84.12	85.31		B.E. (eV)	335.29	337.00	342.14	
used	%At.	64.04	35.96	1.78	%At.	76.03	13.26	10.71	5.74
1%Pd ₈ Au ₂ @HHT	B.E. (eV)	83.84	85.04		B.E. (eV)	335.68	338.00	347.03	
used	%At.	57.57	42.43	1.36	%At.	64.60	26.29	9.11	2.46

Catalytic activity. The catalytic performance of PdAu bimetallic catalysts were tested for the FAD reaction, a model reaction for hydrogen generation. The optimized conditions are 30 °C and 1400 rpm using a solution 0.5 M of FA in water and a FA/metal molar ratio of 2000/1. Reaction conditions (metal:substrate ratio, stirring rate) are optimized in order to assess the kinetic regime of the reaction^[27]. In Figure 3, the catalytic activity at different Pd-Au atomic ratio is shown. The activity is calculated as mol of FA reacted on total mol of metal (Au+Pd) per hour (considering the conversion at 5 minutes of reaction).

Monometallic Au exhibited an extremely low activity in FA decomposition (633 h⁻¹) confirming the results of Z. Zhao et al.^[30], while monometallic 1%Pd@HHT showed an activity of 979 h⁻¹. All the bimetallic catalysts displayed an activity superior to the two monometallic counterparts, except for 1%Pd₂Au₈@HHT (878 h⁻¹). The highest initial activity was observed for 1%Pd₆Au₄@HHT (3539 h⁻¹) followed by 1%Pd₄Au₆@HHT (1983 h⁻¹) and 1%Pd₈Au₂@HHT (1502 h⁻¹). Correlating the initial activity and Au:Pd ratio calculated from XPS and TEM-EDX analyses, we were able to correlate the surface properties of the catalysts with their catalytic behaviour. A Volcano plot was obtained from such correlation for exposed and bulk Pd (Table 2, and Figure 5). Furthermore, the activity increases with the amount of Au until a maximum for 1%Pd₄Au₆@HHT. It was reported in the literature that a PdAu alloy with this metal atomic ratio possesses a perfect balance between the lattice and the ligand effect^[18,19]. In addition, these four catalysts showed an activity for this reaction higher than most of the catalysts present in the literature (Table S1).

Considering the FA conversion at 2 h of reaction, 1%Pd₄Au₆@HHT exhibited the best performance after 2 h of reaction (FAD of 73%), while Au the worst one (FAD <10%) (Figure 6). Despite the initial activity of 1%Pd₈Au₂@HHT was about 2.5 times lower than the one of 1%Pd₄Au₆@HHT, these two catalysts showed a similar conversion from 30 min of reaction and 1%Pd₈Au₂@HHT reached a FAD conversion of 68%. In order to determine the selectivity of the reaction, the gas phase was analysed connecting the reactor with an on-line micro-GC to evaluate the CO/CO₂ ratio. The product detected in the gas phase at 2 h of reaction for the alloyed bimetallic catalysts was only CO₂

without the presence of CO, showing a selectivity >99% for H₂, while 1%Pd@HHT catalyst exhibited 77% selectivity to this product. The high selectivity of the systems can permit the application of the considered bimetallic catalysts in hydrogen fuel cell. Indeed, carbon monoxide is the main issue for the development of this technology and it has to be lower than 10 ppm^[31].

An extremely important feature of a catalyst is the durability to be industrially attractive. For this reason, stability tests were performed on catalysts that showed the best conversion at 2 h (1%Pd₆Au₄@HHT and 1%Pd₈Au₂@HHT). The obtained results were compared with the monometallic palladium (Figure 7). Recycling tests were performed by filtering the catalyst without any further treatment. According to previous studies, palladium catalyst quickly deactivates after the first run (Figure 7a)^[32]. This deactivation is probably due to coalescence and agglomeration of the particles, in fact the average particle size increase from 3.0 to 4.7 nm. In addition, the poor selectivity of the monometallic Pd catalysts generated CO thus poisoning the Pd active sites^[14,33]. On the contrary, the catalysts that show the highest conversion at 2 h, i.e., 1%Pd₆Au₄@HHT and 1%Pd₈Au₂@HHT, exhibit a good stability up to 6 cycles of reaction (Figure 7 b-c). The initial increase in the conversion trend can be due to the partial removal of PVA used during NPs synthesis, which can block some active sites^[34], or the partial reduction of oxidized Pd, present in the fresh catalyst, during the reaction (Table 3). Moreover, GC analyses showed that also selectivity remained constant.

To elucidate the reasons for the enhanced stability observed for the bimetallic catalysts, STEM analysis performed on the used 1%Pd₈Au₂@HHT and 1%Pd₆Au₄@HHT (Figure 8-9) did not show significant modifications of the catalyst morphology. The 1%Pd₈Au₂@HHT fresh catalyst has a mean particle size of 3.5 nm, while the used one 3.9 nm. The analysis performed on 1%Pd₆Au₄@HHT shows a mild increment of particle size from 2.9 to 3.1 nm for the fresh and used catalysts, respectively (Figure 8). Moreover, comparing the Au/Pd atomic ratio of fresh and use catalyst (Table 2, row 5-6 and 8-9), no substantial changes were observed hence, confirming the results in stability and selectivity over more runs.

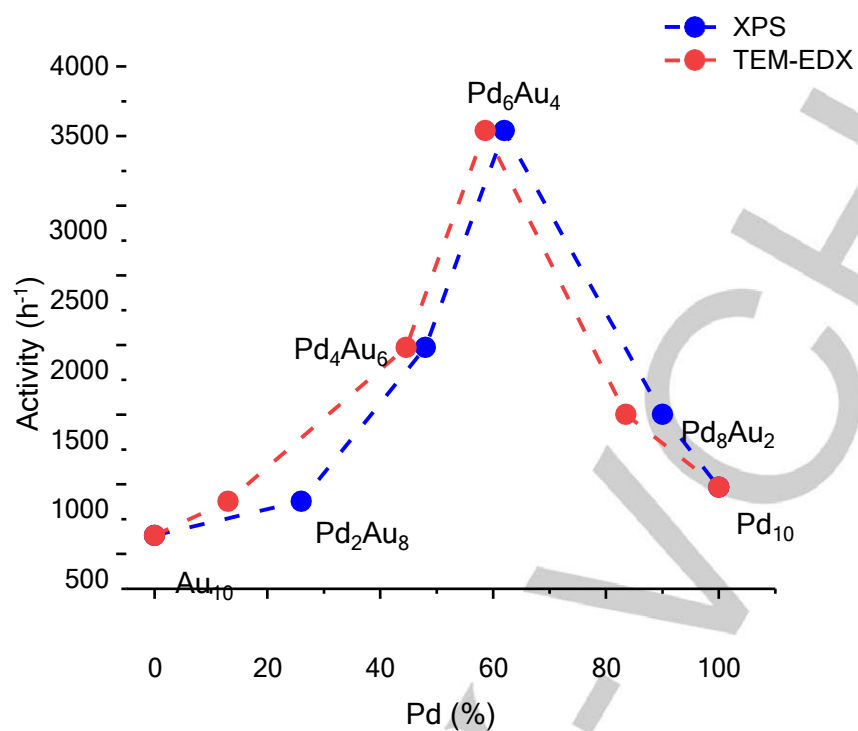


Figure 5. Dependence of the FAD initial activity on the different Pd:Au atomic ratio calculated from XPS (exposed, blue) and TEM-EDX (bulk, red) analyses.

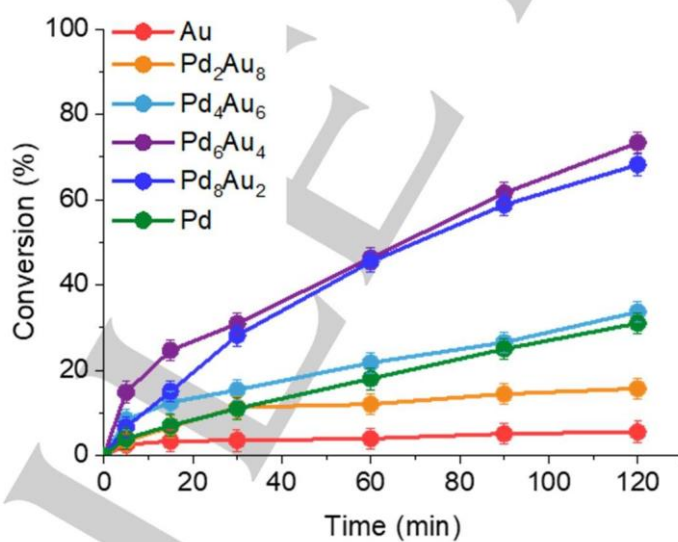


Figure 6. Conversion as a function of reaction time of the different 1%PdxAuy@HHT catalysts for the liquid phase dehydrogenation reaction of FA under mild condition.

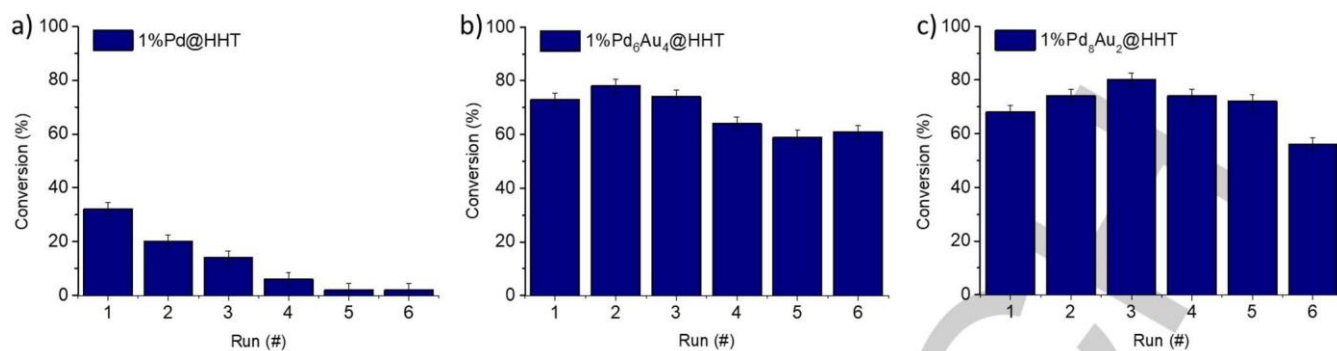


Figure 7. Recycling tests a) monometallic 1%Pd@HHT b) 1%Pd₆Au₄@HHT c) 1%Pd₈Au₂@HHT.

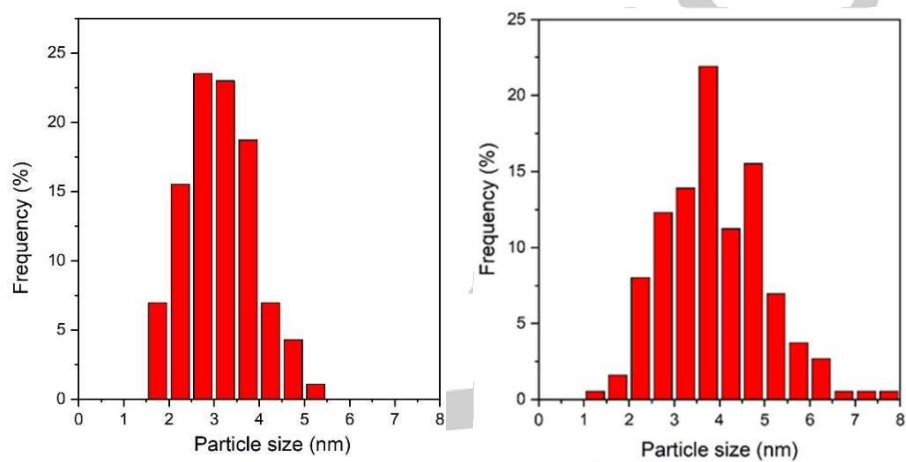


Figure 8. Average particle size distribution of a) used 1%Pd₆Au₄@HHT and b) used 1%Pd₈Au₂@HHT

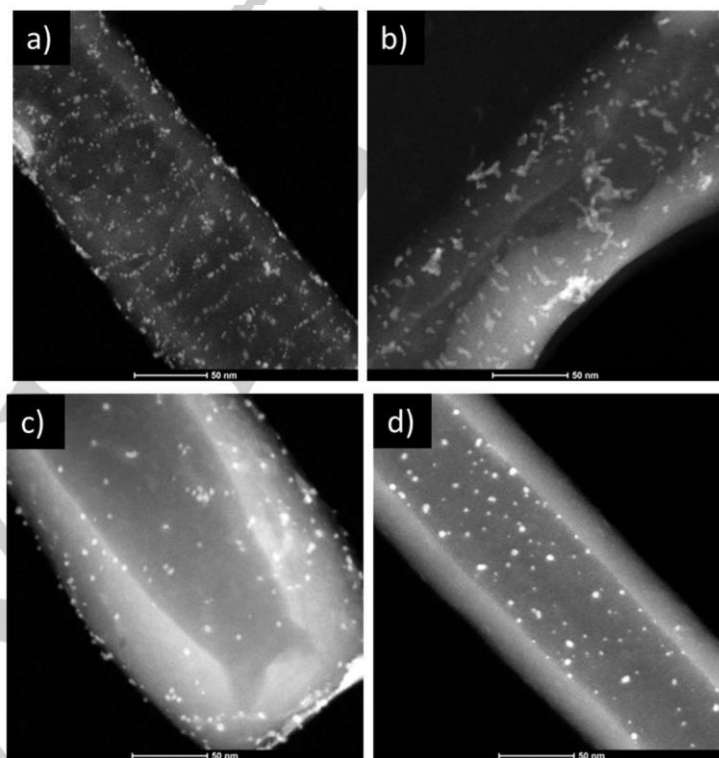


Figure 9. STEM-HAADF images of a) 1%Pd₆Au₄@HHT fresh b) 1%Pd₆Au₄@HHT used c) 1%Pd₈Au₂@HHT fresh and d) 1%Pd₈Au₂@HHT used

DFT study. DFT studies were performed in order to elucidate the superior resistance to sinter and catalytic behaviour of our bimetallic catalysts compared to the monometallic ones (activity and selectivity towards H₂). For this reason, two monometallic (Au₁₅, Pd₁₅; Figure S3-4) and one bimetallic (Pd₉Au₆; Figure S5) clusters on graphitic surfaces were optimized. Pd₉Au₆ is equivalent in Au/Pd atomic ratio of the most promising catalyst, Pd₆Au₄ in line with the results obtained from TEM-EDX analyses. Nanoparticles are dynamic systems that rapidly change their local atomic structure, chemical state and crystallinity under operating condition^[35-38]. We considered clusters' reconstruction energies in both initial (FA adsorption) and final (products desorption) steps to ensure comparability between the energy profiles. Indeed, small NPs are fluxionable^[39] and present a relatively large number of low-energy-lying configurations interconvertible under the reaction conditions considered^[40].

In order to select the most active site for FA adsorption, CO was selected as a probe molecule. CO is a non-desirable intermediate in the HCOOH decomposition mechanism and therefore, simulations will inform the worst-case scenario, i.e., active sites avoid for CO adsorption. We adopted this approach to avoid undertaking reaction mechanisms simulations on all possible sites. Instead, carbon monoxide was brought to all non-equivalent adsorption sites on the clusters and the whole system was relaxed. Carbon monoxide prefers bonding on the metal atoms rather than at the interface between the cluster and the support. This may be attributed to the interaction of the O-lone pair electrons with the inactive π -conjugation of the support^[41]. Then, formic acid was brought and relaxed on the most favorable CO adsorption site with diverse orientations. We selected the most stable adsorption configurations of each structure to perform the subsequent FA decomposition reaction steps. Every elementary step was analysed, resulting in the energy profile in Figure 10. Au is not able to chemically bind FA, in accordance with the poor catalytic activity showed in our experimental results (Figure 5 and 6), therefore it is not included in Figure 10.

The adsorption of FA is exothermic for both Pd and Pd₉Au₆, showing a total energy (E_{tot}) of -2.669 and -7.935 eV, respectively (Figure 11a and 12a). These values can be divided into two different contributions: the first one derives from the reconstruction of the metal atoms during the interaction of the NP with FA (E_{rec}), while the second one describes the adsorption of the substrate (E_{ads}) on the reconstructed cluster. The extremely negative value of energy found for Pd₉Au₆ was mainly due to the NP reconstruction upon FA adsorption, where the metal atoms reached a more stable conformation ($E_{\text{rec}} = -6.775$ eV). A different behaviour was found for monometallic Pd. The contributions of the reconstruction energy and the adsorption energy are similar ($E_{\text{rec}} = -1.043$ eV). This ability of the bimetallic NP to stabilize FA can also explain the superior reactivity and durability of the bimetallic catalysts, in particular, the 1%Pd₆Au₄@HHT catalyst showed in the experimental results, i.e. activity of 3539 h⁻¹, conversion of 73% after 2h and an excellent stability over 6 runs of reaction.

Following the Pd pathway, two different intermediates can be observed. The first and less stable one is obtained from the cleavage of C-H bond forming COOH* intermediate ($E_{\text{R}} = 0.208$ eV, Figure 11b), while the second intermediate, HCOO*, shows an E_{R} of 0.112 eV (Figure 11d). The two intermediates can now decompose following two different pathways forming carbon dioxide and hydrogen or leading to co-adsorbed carbon monoxide and hydroxyl. Both pathways are exothermic, although the formation of carbon dioxide is favoured by an E_{R} of -0.791 eV (Figure 11e) that is 0.227 eV lower than the second path (Figure 11c). These competitive pathways confirm the presence of both carbon monoxide and carbon dioxide observed in the experimental tests.

The formation of HCOO* and COOH* intermediates on Pd₉Au₆ is exothermic (-0.688 eV and -0.128 eV, respectively; Figure 12 b-d). We also observe that the most stable species is also HCOO* but, on this catalyst, the difference with COOH* is 0.560 eV, which already eases the competition towards HCOO*. Considering again both possible pathways in the following decomposition step, the favourite route is the formation of carbon dioxide and atomic hydrogen adsorbed on the surface ($E_{\text{R}} = -0.271$ eV, Figure 12e) differing from the undesired pathway of 0.230 eV (Figure 12c). The releasing of the molecular species from the surface of the catalyst is for both pathways endothermic but, in the case of carbon dioxide and hydrogen the energy barrier is lower ($E_{\text{B}} = 1.511$ eV), whereas for carbon monoxide and water the energy gap to overcome is 2.582 eV. The energy difference between the preferred CO₂ path and the one forming CO explains the selectivity between monometallic Pd catalyst and the bimetallic Pd₉Au₆ systems. This result is in agreement with the DFT study of J. Cho et al. where the importance of the second metal effect in a core shell structure is highlighted. It was claimed that adding a second metal, such as Au, as core of a core-shell Pd structure can enhance the rate of this reaction and also suppress the dehydration pathway^[16].

In order to reveal the selectivity, reactivity and superior stability of Au₆Pd₉ supported nanoparticles, we investigated the electronic structure of all the three supported systems on graphene. We calculated the partial charge density of the supported clusters from the gas phase with the same morphology. Upon adhesion, the ~~There is an obvious~~ electron density rearranges ~~upon nanoparticle deposition, indicated~~ as shown from the electron density depletion (blue) and gain (yellow) iso-surfaces in Figure 13. In Au system, the arrangement places the electrons at the core of the nanoparticle as previously observed^[42]. The Pd nanoparticle localizes its electron density away from the surface while on Au₆Pd₉ the electron density is relocated at the interface between the nanoparticle and the support. This suggests a stronger interaction with the support in the bimetallic system in full agreement with the results obtained in the experimental part, where the bimetallic catalysts showed a durability superior than monometallics.

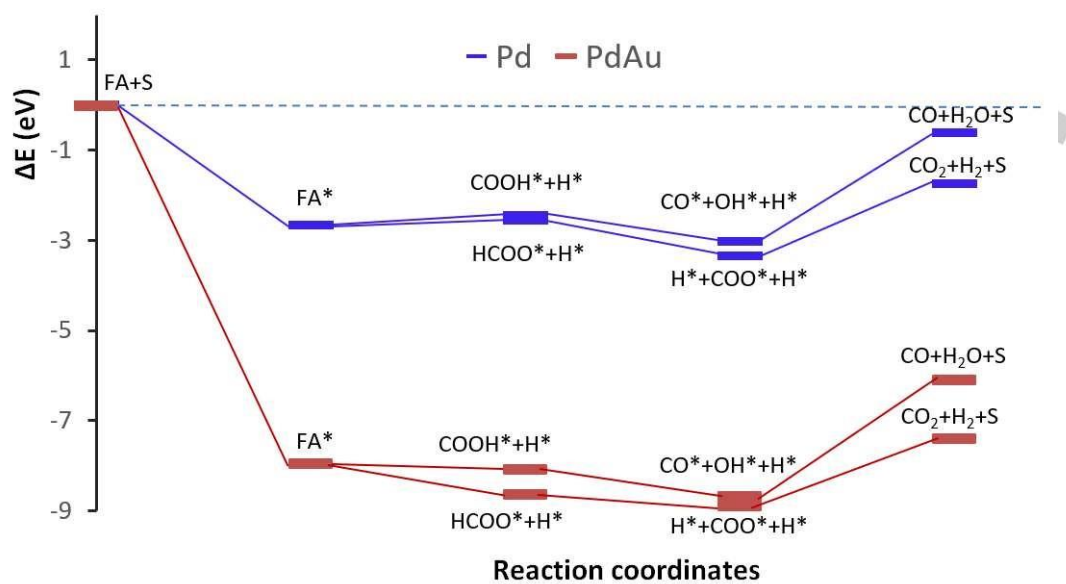


Figure 10. Energy profile for the different pathways of formic acid decomposition on Pd_{15} (blue) and Pd_9Au_6 (red) clusters. The energy of the initial state $\text{FA} + \text{S}$ was calculated as the energy of the initial cluster structure (S) and the energy of formic acid (FA) isolated. Final state S is the reconstructed structure. The final S can reconstruct to the initial S spontaneously. * indicates the adsorbed species.

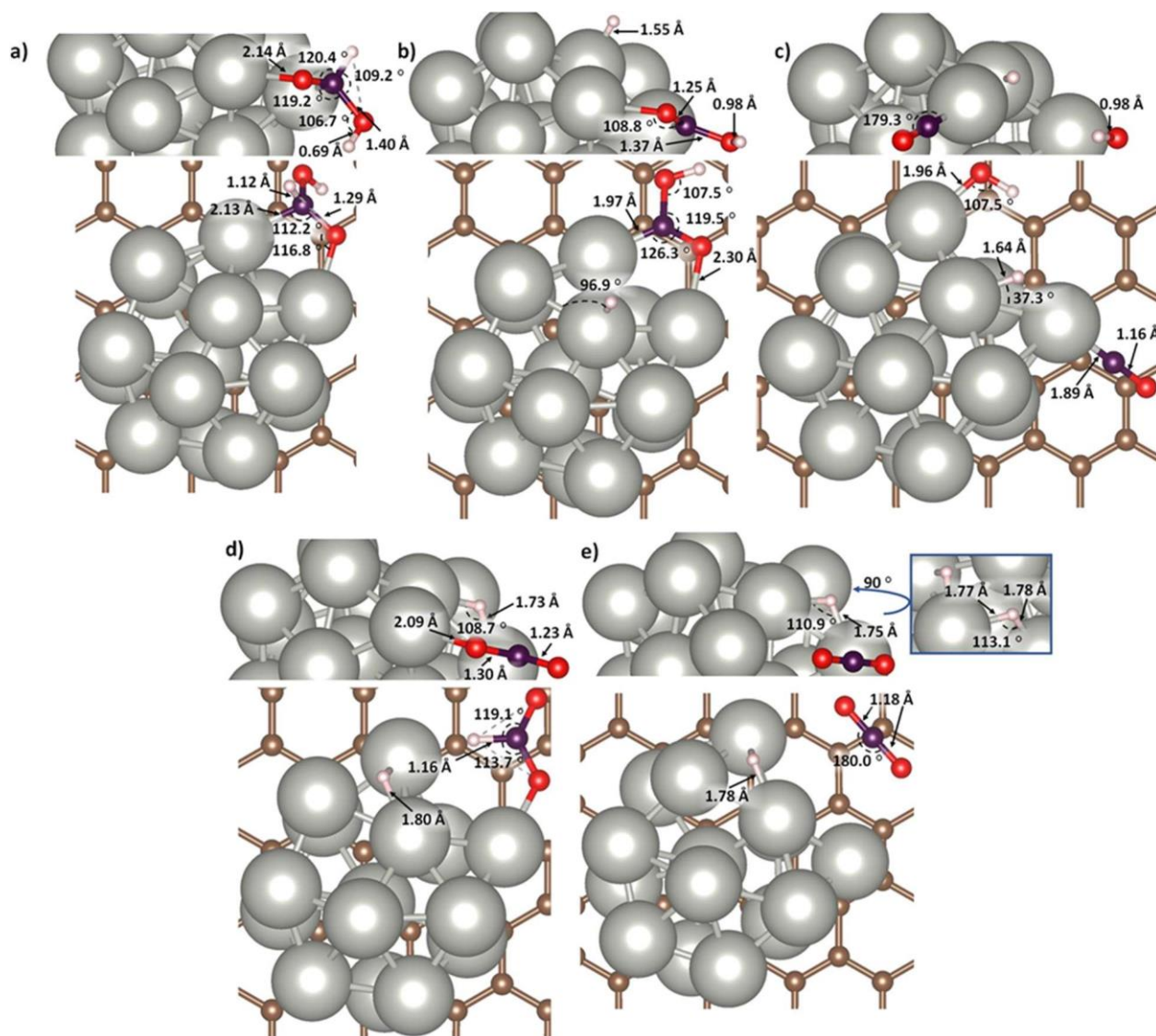


Figure 11. Top and side views of the optimized elementary steps on Pd_{15} cluster; (a) FA adsorbed on the cluster, (b) COOH and H adsorbed after the dissociation of the C-H bond, (c) CO, H and OH adsorbed after the dissociation of the C-OH bond, (d) HCOO and H adsorbed after the dissociation of the O-H bond and (e) H and H adsorbed on the cluster after the dissociation of C-H bond. CO_2 is more stable in gas phase than adsorbed. The inset in this figure is referred to a rotation of 90° on the z axis showing the second H adsorbed on the Pd. Inset shows the distances and angles of interest. Carbon atoms are represented in brown, palladium in silver, oxygen in red, hydrogen in white and the carbon atoms of formic acid in purple.

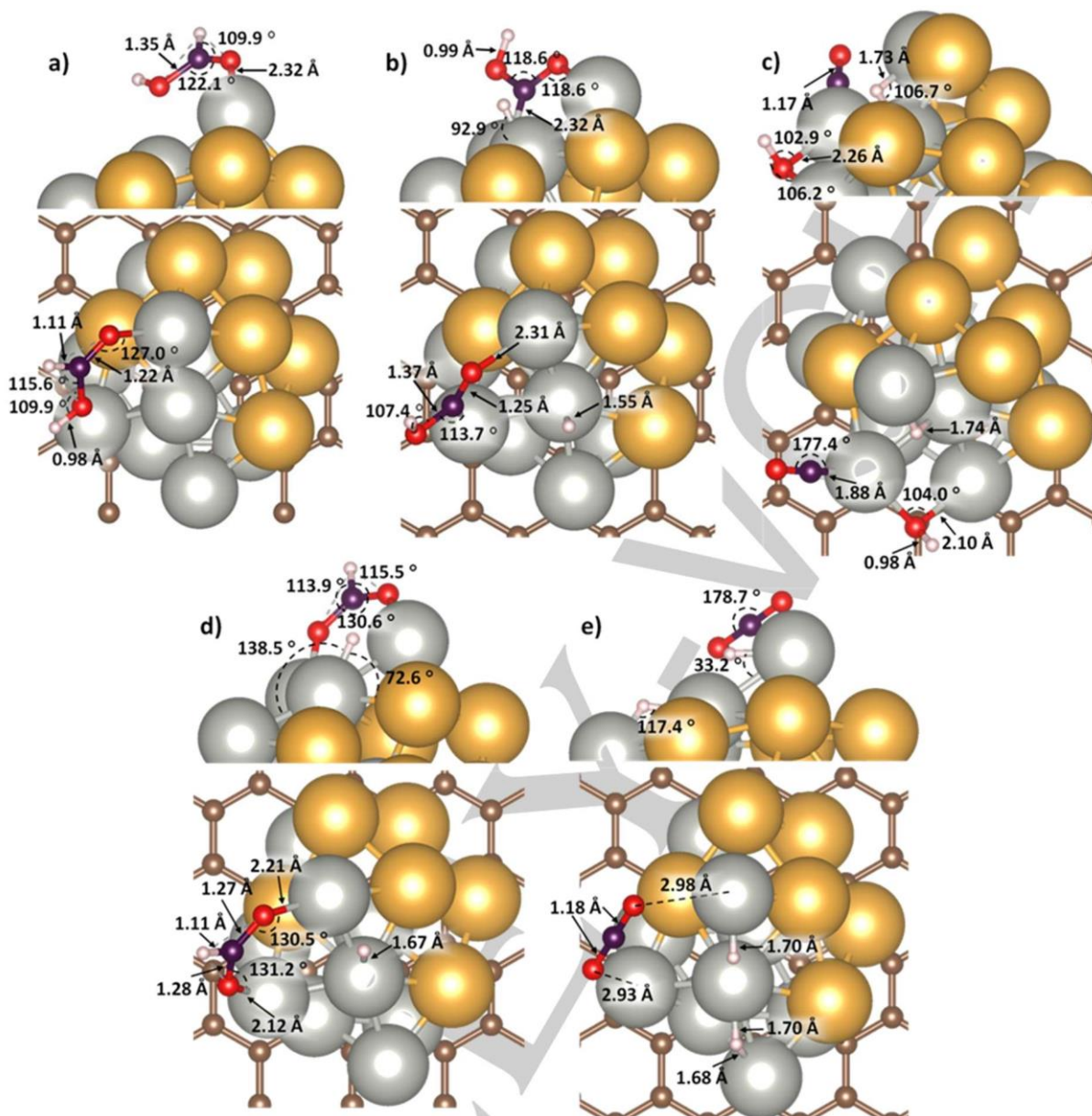


Figure 12. Top and side views of the optimized elementary steps on Pd_9Au_6 cluster; (a) FA adsorbed on the cluster, (b) COOH and H adsorbed after the dissociation of the C-H bond, (c) CO, H and OH adsorbed after the dissociation of the C-OH bond, (d) HCOO and H adsorbed after the dissociation of the O-H bond and (e) H and H adsorbed on the cluster after the dissociation of C-H bond. CO_2 is more stable in gas phase than adsorbed. Insets show distances and angles of interest. Carbon atoms are represented in brown, gold atoms in gold, palladium in silver, oxygen in red, hydrogen in white and the carbon atoms of formic acid in purple.

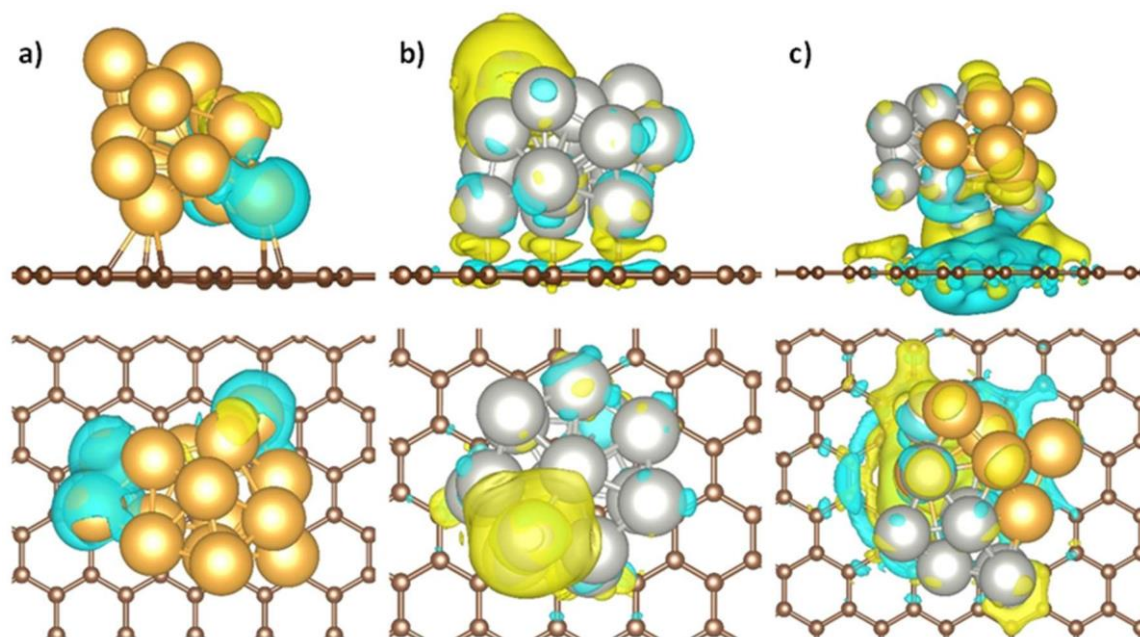


Figure 13. Side and top view of the partial charge density analysis upon: a) Au_{15} , b) Pd_{15} and c) Au_6Pd_9 . Yellow and blue iso-surfaces denote gain and depletion of electron density. Gold, silver and khaki spheres represent gold, palladium and carbon, respectively

Conclusion

In conclusion, this work combines DFT and experimental data to disclose the role of gold in enhancing activity, selectivity and stability of palladium catalyst during the formic acid decomposition. PdAu catalysts were synthesised using sol-immobilization technique with a systematic variation of Au to Pd molar ratio, obtaining in the majority cases an alloy with an enrichment of palladium on the surface confirmed by XPS, STEM-HAADF and STEM-XEDS analyses. The activity plot showed a typical volcano trend with a maximum for 1% Pd_6Au_4 @HHT catalyst (3539 h^{-1}). An increasing in conversion at 2 h of reaction is observed for most of the bimetallic systems, in particular for 1% Pd_6Au_4 @HHT and 1% Pd_8Au_2 @HHT (73% and 68%, respectively). Moreover, an inhibition of the dehydration pathway was observed for gold-containing catalysts. 1% Pd_6Au_4 @HHT and 1% Pd_8Au_2 @HHT also showed an excellent stability during six consecutive runs, whereas 1% Pd @HHT rapidly deactivates because of leaching, coalescence and CO-poisoning. DFT models of Pd_{15} , Au_{15} and Pd_9Au_6 clusters were then employed to better understand the beneficial effect of gold observed in the experimental results. While Au_{15} was not able to interact with FA, Pd_{15} and Pd_9Au_6 could exothermically adsorb the substrate according to our observations. Nonetheless, the Pd_9Au_6 catalyst showed a more exothermic adsorption of formic acid than Pd_{15} , confirming the superior activity of the bimetallic system. Moreover, considering the pathways observed for both systems, the Pd_9Au_6 favourite route was the formation of carbon dioxide and hydrogen, while Pd_{15} can follow both the dehydrogenation and dehydration pathways, in agreement with the analyses performed on the products. Additionally, as far as we know this is the first study demonstrating a stronger interaction between the bimetallic

system and the support confirming the excellent durability results observed in the experimental part, using the analysis of the electronic structures of the different modelled clusters. These results demonstrate that alloying Pd with Au facilitates the synthesis of active, highly selective and durable catalysts for the sustainable formation of hydrogen from formic acid decomposition at mild conditions.

Experimental Section

Materials and chemicals. Sodium tetrachloroaurate(III) dihydrate ($\text{NaAuCl}_4 \cdot 2\text{H}_2\text{O}$, 99.99 %), sodium tetrachloropalladate (II) (Na_2PdCl_4 , 99.99 %), sodium borohydride (NaBH_4 , 99.99 %) and poly(vinyl alcohol) (PVA, average molar weight 10,000, 87-89 % hydrolyzed) were used without any pre-treatment for the catalysts synthesis and they were purchased from Sigma-Aldrich (Haverhill, MA, USA). All the catalytic tests were carried out using Formic acid ($\geq 95\%$, Sigma-Aldrich) and deionised water. CNFs PR24-HHT (High Heat Treated carbon nanofiber) were obtained from Applied Science Company (Cedarville, OH, USA).

Catalysts preparation. Following a typical sol immobilization procedure^[43], the catalyst was prepared by adding the solution of the precursor salt (K_2PdCl_4 , $\text{NaAuCl}_4 \cdot 2\text{H}_2\text{O}$; Tab. 4) to 100 mL of H_2O . Afterwards, the PVA (Metal/PVA=1/0.5 (wt/wt)) was added. Then, a fresh aqueous solution of NaBH_4 ($M/\text{NaBH}_4=1/8 \text{ mol/mol}$) was inserted at once. After 30 minutes under vigorous stirring 1 g of HHT nanofibers was added in order to support the metal colloidal solution. By using sulphuric acid, the suspension was acidified to pH 2 and stirred for 30 min in order to ensure the full immobilization of the nanoparticles on the support^[24]. The solid was filtered, washed with 1 L of H_2O and dried in oven at 80°C for 1 day.

Table 4. Summary of the amount of the metals for the preparation of the sol.

Pd-Au Ratio	Pd (mmolx10 ⁻²)	Au (mmolx10 ⁻²)
1%Pd@HHT	9.40	-
1%Pd ₈ Au ₂ @HHT	6.42	1.61
1%Pd ₆ Au ₄ @HHT	4.21	2.80
1%Pd ₄ Au ₆ @HHT	2.49	3.73
1%Pd ₂ Au ₈ @HHT	1.12	4.47
1%Au@HHT	-	5.08

Catalytic tests. FA dehydrogenation: Liquid-phase Formic acid decomposition was carried out in a two-necked 100 mL round-bottom flask placed in a water bath equipped with a magnetic stirrer and a reflux condenser. Typically, 10 mL of an aqueous solution 0.5 M of FA was placed in the reactor and the reaction temperature was set at 30 °C. The Formic Acid/metal molar ratio is 2000:1 and once the solution reached the desired temperature, the solution was stirred at 1400 rpm. At these experimental conditions we are operating under kinetic regime^[27]. Recycle tests were performed on the most active catalysts using 25 mL of an aqueous solution of FA (0.5 M) in a 250 mL round-bottom flask at the same experimental conditions of the reaction previously discussed.

Product analysis: Formic acid conversion was analysed using high-performance liquid chromatography (HPLC). In particular, an H⁺ chromatographic column was used (Alltech OA- 10,308, 300 mm_7.8 mm) with UV detector settled at 210 nm. Liquid samples were withdrawn periodically (200 µL) and diluted to 5 mL with H₃PO₄ solution (0.1 wt %) which was also the eluent of the analysis. The isocratic eluent flow was set at 0.4 mL min⁻¹. Analysis of the gas was executed using an online micro-gas chromatograph (Agilent 3000A) after 2 hours of reaction. The device is equipped with a TCD detector and two different columns: (a) a molecular sieve module and (b) an OV-1 module (stationary phase of polydimethylsiloxilane), with a detection limit of CO below 5 ppm. CO and CO₂ were measured by mean of calibration curves created from commercial standards.

Catalyst characterization. TEM: High angle annular dark-field (HAADF) scanning transmission electron microscopy (STEM) imaging and energy dispersive X-ray spectroscopy (EDX) analysis were performed on a Themis300 transmission electron microscope (ThermoFisher Scientific), equipped with probe aberration corrector and Super-X EDX detectors. For these analyses, catalysts were sonicated in ethanol and dropped on Cu TEM grids, covered with holey carbon film. The particle size distribution was determined by fitting ellipsoid shapes to the metal particles using ImageJ software, by which more than 200 nanoparticles were measured to get good statistical representation for each catalyst.

XPS: Thermo Scientific K-alpha+ spectrometer was used for XPS measurements. The samples were analysed using a monochromatic Al X-Ray source operating at 72 W, with the signal averaged over an oval-shape area of 600x400 µ. Data were recorded at 150 eV for survey scans and 40 eV for high resolution (HR) scans with a 1 eV and 0.1 eV step size, respectively. CASAXPS (v2.3.17 PR1.1) was used for the analysis of the data, using Scofield sensitivity factors and energy exponent of -0.6.

Computational method. Periodic plane-wave density functional theory (DFT) calculations were performed using the Vienna ab initio simulation package (VASP).^[44,45] The exchange-correlation was described by the spin-polarized revised Perdew-Burke-Ernzerhof (rPBE) method of the generalized gradient approximation (GGA) with a plane-wave kinetic cutoff energy of 450 eV.^[46] Non-spherical contributions correlated to the gradient of the density are integrated in the projector augmented wave (PAW).^[47-49] The long-range interaction was characterized by the DFT-D3 method of

Grimme with zero-damping.^[50] The solvent effect of water was also considered by an implicit polarized continuum model (PCM), which describes the interaction between a solute and solvent into the plane-wave DFT.^[51,52] The optimized convergence threshold of internal forces and electronic relaxation was set to 0.01 eV/Å and 10⁻⁷ eV, respectively. A 0.2 Å⁻¹ k-spacing sampled the Brillouin zone with a smearing broadening of 0.1 eV.

The experimental catalysts were modelled by pristine carbon surface decorated with metallic nanoparticles maintaining an equivalent Au:Pd ratio. The optimized lattice parameter of supporting pristine graphene is 2.469 Å, which is in agreement with the benchmark value of 2.46 Å.^[53] All surfaces were represented by a p(8x8) supercell slab model to avoid the interaction between the metal clusters. The expensive exploration of the supported nanoparticles' conformational morphology restricted their size to 15 metallic atoms. To determine the most stable initial shapes and the distribution of species within the NPs, we employed an unbiased genetic algorithm (GA) to explored up to 100 independent structures for each Pd, Au and AuPd clusters, besides moieties that maximized the exposure of the most stable facets, i.e., (111) and those based on previous reports.^[54] We recognized that not all possible configurations were simulated, nevertheless, we proved during the presented research that these clusters are highly dynamic and their reactivity is not related directly to the rigid morphology of the global energy minima's structure.^[55] We added 15 Å of vacuum perpendicular to the carbon slab to avoid any spurious interaction with periodic images. Dipole correction perpendicular to the surface was applied upon deposition of the NPs.

NPs' adhesion energy (E_{Adh}) was calculated as the difference between the combined system and the isolated NP and carbon sheet with the same geometry as the combined system. The molecular adsorption energy (E_{Ads}), which is equivalent to the desorption energy (E_{Des}) was defined as the difference between the combined system and the isolated species, i.e., the desorbed molecular species and the cluster in exactly the same geometry as the last combined models. The final cluster after the desorption step is considered to spontaneously reconstruct to the initial state. The reaction energy (E_{R}) defined as the total energy difference between the final (final adsorbate-NP/C) and the initial states (initial adsorbate-NP/C).

Acknowledgements

A.V. is grateful to Karlsruhe Nano Micro Facility (KNMF) for a long-term Project for supporting the TEM work. X.Huang acknowledges the China Scholarship Council (CSC) for the supporting of her PhD in Karlsruhe Institute of Technology. X. Lu acknowledges the China Scholarship Council and Cardiff University for the overseas student scholarship (CSC No. 201806370221). Via membership of the UK's HPC Materials Chemistry Consortium, which is funded by EPSRC (EP/L000202, EP/R029431), this work used the UK Materials and Molecular Modelling Hub for computational resources, MMM Hub, which is partially funded by EPSRC (EP/T022213/1). We also acknowledge computing time on the facilities at Cardiff University managed by the Advanced Research Computing @ Cardiff (ARCCA).

Keywords: formic acid • PdAu • alloy • stability

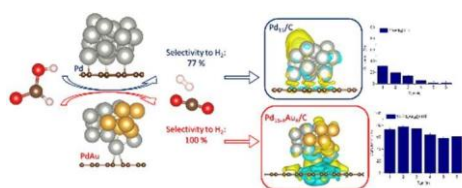
- [1] T. N. Veziroğlu, S. Şahin, *Energy Convers. Manag.* **2008**, 49, 1820-1831.

- [2] P. Nikolaidis, A. Poullikkas, *Renew. Sustain. Energy Rev.* **2017**, *67*, 597-611.
- [3] M. Z. Chen W, L. Z. ouyang, J. W. Liu, X. D. Yao, H. Wang, Z. W. Liu, *J. Power Sources* **2017**, *359*, 400-407.
- [4] I. Shown, A. Ganguly, L. C. Chen, K. H. Chen, *Energy Sci. Eng.* **2015**, *3*, 1-25.
- [5] K. Sordakis, C. Tang, L. K. Vogt, H. Junge, P. J. Dyson, M. Beller, G. Laurenczy, *Chem. Rev.* **2018**, *118*, 372-433.
- [6] H. jin Jeon, Y. M. Chung, *Appl. Catal. B Environ.* **2017**, *210*, 212-222.
- [7] F. Joó, *ChemSusChem* **2008**, *1*, 805-808.
- [8] D. J. Braden, C. A. Henao, J. Heltzel, C. C. Maravelias, J. A. Dumesic, *Green Chem.* **2011**, *13*, 1755-1765.
- [9] J. J. Bozell, G. R. Petersen, *Green Chem.* **2010**, *12*, 539-554.
- [10] E. Iglesia, M. Boudart, *J. Catal.* **1983**, *81*, 204-213.
- [11] Q. Y. Bi, X. L. Du, Y. M. Liu, Y. Cao, H. Y. He, K. N. Fan, *J. Am. Chem. Soc.* **2012**, *134*, 8926-8933.
- [12] D. A. Bulushev, S. Beloshapkin, J. R. H. Ross, *Catal. Today* **2010**, *154*, 7-12.
- [13] M. Gräsemann, G. Laurenczy, *Energy Environ. Sci.* **2012**, *5*, 8171-8181.
- [14] F. Abild-Pedersen, M. P. Andersson, *Surf. Sci.* **2007**, *601*, 1747-1753.
- [15] M. Mavrikakis, J. A. Herron, J. Scaranto, P. Ferrin, S. Li, *ACS Catal.* **2014**, *4*, 4434-4445.
- [16] J. Cho, S. Lee, S. P. Yoon, J. Han, S. W. Nam, K. Y. Lee, H. C. Ham, *ACS Catal.* **2017**, *7*, 2553-2562.
- [17] J. H. Lee, J. Cho, M. Jeon, M. Ridwan, H. S. Park, S. H. Choi, S. W. Nam, J. Han, T. H. Lim, H. C. Ham, C. W. Yoon, *J. Mater. Chem. A* **2016**, *4*, 14141-14147.
- [18] Q. Wang, L. Chen, Z. Liu, N. Tsumori, M. Kitta, Q. Xu, *Adv. Funct. Mater.* **2019**, *29*, 1-7.
- [19] Z. Xing, Z. Guo, X. Chen, P. Zhang, W. Yang, *Catal. Sci. Technol.* **2019**, *9*, 588-592.
- [20] Q. Lv, Q. Meng, W. Liu, N. Sun, K. Jiang, L. Ma, Z. Peng, W. Cai, C. Liu, J. Ge, L. Liu, W. Xing, *J. Phys. Chem. C* **2018**, *122*, 2081-2088.
- [21] J. H. Carter, S. Althahban, E. Nowicka, S. J. Freakley, D. J. Morgan, P. M. Shah, S. Golunski, C. J. Kiely, G. J. Hutchings, *ACS Catal.* **2016**, *6*, 6623-6633.
- [22] D. Liu, Z. Y. Gao, X. C. Wang, J. Zeng, Y. M. Li, *Appl. Surf. Sci.* **2017**, *426*, 194-205.
- [23] Y. Karatas, A. Bulut, M. Yurderi, I. E. Ertas, O. Alal, M. Gulcan, M. Celebi, H. Kivrak, M. Kaya, M. Zahmakiran, *Appl. Catal. B Environ.* **2016**, *180*, 586-595.
- [24] A. Villa, D. Wang, N. Dimitratos, D. Su, V. Trevisan, L. Prati, *Catal. Today* **2010**, *150*, 8-15.
- [25] N. Dimitratos, J. A. Lopez-Sanchez, D. Morgan, A. F. Carley, R. Tiruvalam, C. J. Kiely, D. Bethell, G. J. Hutchings, *Phys. Chem. Chem. Phys.* **2009**, *11*, 5142-5153.
- [26] I. Barlocco, S. Capelli, E. Zanella, X. Chen, J. J. Delgado, A. Roldan, N. Dimitratos, A. Villa, *J. Energy Chem.* **2020**, *52*, 301-309.
- [27] F. Sanchez, M. H. Alotaibi, D. Motta, C. E. Chan-Thaw, A. Rakotomahevitra, T. Tabanelli, A. Roldan, C. Hammond, Q. He, T. Davies, A. Villa, N. Dimitratos, *Sustain. Energy Fuels* **2018**, *2*, 2705-2716.
- [28] F. Sanchez, D. Motta, L. Bocelli, S. Albonetti, A. Roldan, C. Hammond, A. Villa, N. Dimitratos, *C* **2018**, *4*, 26.
- [29] X. Zhu, Q. Guo, Y. Sun, S. Chen, J.-Q. Wang, M. Wu, W. Fu, Y. Tang, X. Duan, D. Chen, Y. Wan, *Nat. Commun.* **2019**, *10*, 1428.
- [30] Z. Zhao, K. N. Heck, P. Limpornpipat, H. Qian, J. T. Miller, M. S. Wong, *Catal. Today* **2019**, *330*, 24-31.
- [31] D. Mellmann, P. Sponholz, H. Junge, M. Beller, *Chem. Soc. Rev.* **2016**, *45*, 3954-3988.
- [32] F. Sanchez, D. Motta, A. Roldan, C. Hammond, A. Villa, N. Dimitratos, *Top. Catal.* **2018**, *61*, 254-266.
- [33] H. Sakai, T. Nakajima, N. Yoshida, S. Kishimoto, *React. Kinet. Catal. Lett.* **1982**, *19*, 297-301.
- [34] S. Campisi, C. E. Chan-Thaw, D. Wang, A. Villa, L. Prati, *Catal. Today* **2016**, *278*, 91-96.
- [35] A. Bergmann, B. Roldan Cuenya, *ACS Catal.* **2019**, *9*, 10020-10043.
- [36] C. Chizallet, P. Raybaud, *Catal. Sci. Technol.* **2014**, *4*, 2797-2813.
- [37] S. W. Chee, J. M. Arce-Ramos, W. Li, A. Genest, U. Mirsaidov, *Nat. Commun.* **2020**, *11*, 2133.
- [38] J. Dean, M. G. Taylor, G. Mpourmpakis, *Sci. Adv.* **2019**, *5*, eaax5101.
- [39] A. S. Crampton, M. D. Rötzer, C. J. Ridge, F. F. Schweinberger, U. Heiz, B. Yoon, U. Landman, *Nat. Commun.* **2016**, *7*, 10389.
- [40] H. Zhai, A. N. Alexandrova, *J. Phys. Chem. Lett.* **2018**, *9*, 1696-1702.
- [41] I. Barlocco, S. Capelli, X. Lu, S. Tumati, N. Dimitratos, A. Roldan, A. Villa, *Nanoscale* **2020**, 22768-22777.
- [42] A. Roldán, J. M. Ricart, F. Illas, G. Pacchioni, *Phys. Chem. Chem. Phys.* **2010**, *12*, 10723-10729.
- [43] S. Campisi, D. Ferri, A. Villa, W. Wang, D. Wang, O. Kröcher, L. Prati, *J. Phys. Chem. C* **2016**, *120*, 14027-14033.
- [44] G. Kresse, J. Furthmüller, *Comput. Mater. Sci.* **1996**, *6*, 15-50.
- [45] T. Bučko, J. Hafner, S. Lebegue, J. G. Ángyán, *J. Phys. Chem. A* **2010**, *114*, 11814-11824.
- [46] B. Hammer, L. B. Hansen, J. K. Nørskov, *Phys. Rev. B* **1999**, *59*, 7413-7421.
- [47] J. P. Perdew, K. Burke, M. Ernzerhof, *Phys. Rev. Lett.* **1996**, *77*, 3865-3868.
- [48] G. Kresse, D. Joubert, *Phys. Rev. B* **1999**, *59*, 1758-1775.
- [49] P. E. Blöchl, O. Jepsen, O. K. Andersen, *Phys. Rev. B* **1994**, *49*, 16223-16233.
- [50] S. Grimme, S. Ehrlich, L. Goerigk, *J. Comput. Chem.* **2011**, *32*, 1456-1465.
- [51] K. Mathew, V. S. C. Kolluru, S. Mula, S. N. Steinmann, R. G. Hennig, *J. Chem. Phys.* **2019**, *151*, 234101.
- [52] K. Mathew, R. Sundaraman, K. Letchworth-Weaver, T. A. Arias, R. G. Hennig, *J. Chem. Phys.* **2014**, *140*, DOI 10.1063/1.4865107.
- [53] A. K. Geim, *Science (80-.)* **2009**, *324*, 1530 LP - 1534.
- [54] R. L. Johnston, *Dalt. Trans.* **2003**, 4193-4207.

- [55] G. Sun, J. T. Fuller, A. N. Alexandrova, P. Sautet, *ACS Catal.* **2021**, *11*, 1877-1885.

WILEY-VCH

Entry for the Table of Contents



DFT and experimental data were employed to disclose the role of gold in palladium-based catalyst during the aqueous-phase formic acid decomposition. Pd₆Au₄ and Pd₉Au₆ showed the best catalytic properties: high H₂ selectivity and increased stability. DFT calculations on Pd₁₅, Au₁₅ and Pd₉Au₆ clusters supported on a graphitized carbon were simulated. Dehydrogenation and dehydration pathways were studied and, for Pd₉Au₆ the most exothermic route was the dehydrogenation. Moreover, Pd₉Au₆ exhibited a stronger interaction with the carbon proving its superior stability.